Weierstraß-Institut
für Angewandte Analysis und Stochastik

im Forschungsverbund Berlin e.V.

Preprint ISSN 0946 – 8633

Experimental and numerical model study of the limiting current in a channel flow cell with a circular electrode

J. Fuhrmann[1], H. Zhao[1], E. Holzbecher[1], H. Langmach[1],

M. Chojak[2], R. Halseid[2,3], Z. Jusys[2], R. J. Behm[2]

[1] Weierstrass Institute for Applied Analysis and Stochastics
Mohrenstr. 39, 10117 Berlin, Germany
email: {fuhrmann|zhao|holzbecher|langmach}@wias-berlin.de

[2] Institute of Surface Chemistry and Catalysis, Ulm University
89069 Ulm, Germany
email: {malgorzata.chojak|zenonas.jusys|juergen.behm}@uni-ulm.de

[3] StatoilHydro ASA
NO-0246 Oslo, Norway
email: halseid@hotmail.com

submitted: Feb. 17, 2008

No. 1301
Berlin 2008

2000 *Mathematics Subject Classification.* 35K20, 65N99.

Key words and phrases. limiting current, Finite Volume Method, boundary layer, parameter estimation.

Edited by
Weierstraß-Institut für Angewandte Analysis und Stochastik (WIAS)
Mohrenstraße 39
10117 Berlin
Germany

Fax: + 49 30 2044975
E-Mail: preprint@wias-berlin.de
World Wide Web: http://www.wias-berlin.de/

Experimental and numerical model study of the limiting current in a channel flow cell with a circular electrode

J. Fuhrmann[1], H. Zhao[1], E. Holzbecher[1], H. Langmach[1], M. Chojak[2], R. Halseid[2,3], Z. Jusys[2], and R. J. Behm[2]

Abstract. We describe first measurement in a novel thin-layer channel flow cell designed for the investigation of heterogeneous electrocatalysis on porous catalysts. For the interpretation of the measurements, a macroscopic model for coupled species transport and reaction, which can be solved numerically, is feasible. In this paper, we focus on the limiting current. We compare numerical solutions of a macroscopic model to a generalization of a Leveque-type asymptotic estimate for circular electrodes, and to measurements obtained in the aforementioned flow cell. We establish, that on properly aligned meshes, the numerical method reproduces the asymptotic estimate. Furthermore, we demonstrate, that the measurements are partially performed in the sub-asymptotic regime, in which the boundary layer thickness exceeds the cell height. Using the inlet concentration and the diffusion coefficient from literature, we overestimate the limiting current. On the other hand, the use of fitted parameters leads to perfect agreement between model and experiment.

1. Introduction

Thin-layer channel flow cells are widely used in (electro)analytical chemistry as electrochemical detectors [**1, 2**]. Due to their small working volume (in the range of microliters), a fast signal response can be achieved and utilized for flow-injection analysis [**3**]. Alternatively, the concentration of electro-active species can be monitored on-line under continuous flow of the analyte. In addition to measuring the analyte concentration via the Faradaic current, the formation of electro-active species on the working electrode ('generator') can be detected and quantified by a second electrode ('collector'), e.g., by positioning two adjacent electrode stripes across the flow channel [**4, 5**]. In many studies, the transport characteristics of thin-layer flow cells have been modeled e.g., for a quantitative evaluation of reaction kinetics [**6**].

In contrast to their wide use in electroanalysis, thin-layer flow cells are much less often applied in electrocatalysis research, despite of their considerable potential for these applications. The latter is demonstrated by a number of model studies on electrocatalytic reactions, including e.g., methanol oxidation reaction (MOR) [**7, 8, 9**] and oxygen reduction reaction(ORR) [**10, 11, 12, 13, 14**]. These studies demonstrated the importance of operating under controlled and continuous electrolyte flow. A particular advantage of flow cell measurements compared to other hydrodynamic electrochemical techniques such as rotating disk electrode measurements [**15, 16**], is their capability for rapid electrolyte exchange, which is important for transient measurements [**13**], and their ability to work at elevated temperatures and pressures [**10, 11**]. The potential of thin-layer flow cell measurements for electrocatalysis research was further extended by a recently developed dual thin-layer flow cell design [**17**], which allows the on-line and *in-situ* detection of volatile reaction products [**18, 19**] and of adsorbed reaction intermediates/products by connection to a mass spectrometer or to an infrared spectrometer [**18, 19, 20, 21**]. Alternatively, a second collector electrode can be included for electroactive product detection [**12, 13, 14**].

A quantitative interpretation of the measured data is possible on the basis of mathematical models describing the coupled electrolyte flow, transport and the ongoing reactions [**16**]. Often a description by partial differential equations is utilized [**5**]. In the general case, where boundary layer theory is not

[1]Weierstrass Institute for Applied Analysis and Stochastics, Mohrenstr. 39, 10117 Berlin, Germany
email: {fuhrmann|zhao|holzbecher|langmach}@wias-berlin.de
[2]Institute of Surface Chemistry and Catalysis, Ulm University, 89069 Ulm, Germany.
email: {malgorzata.chojak|zenonas.jusys|juergen.behm}@uni-ulm.de
[3]StatoilHydro ASA, NO-0246 Oslo, Norway
email: halseid@hotmail.com

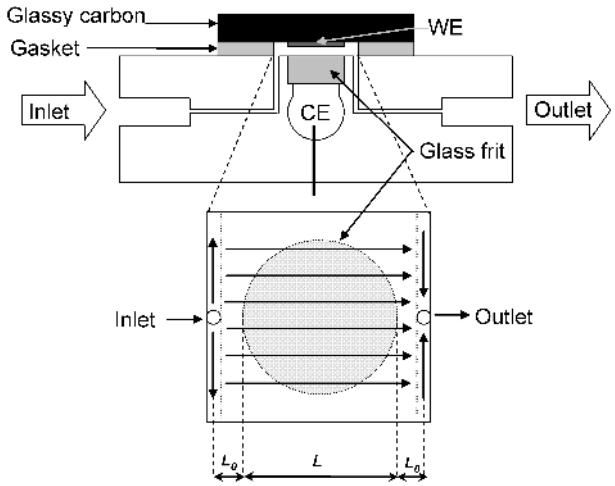

FIGURE 1. Schematic of the flow cell, WE-working electrode, CE-counter electrode

applicable, and analytical solutions of the corresponding partial differential equations are not available, numerical methods have to be used in order to obtain approximate solutions (see, e.g., refs. [**22, 23, 24**]). In this paper, we present a simulation approach based on the finite volume method, which can be considered as a generalization of the finite difference method to unstructured meshes. This method allows for more geometrical flexibility with the limitation that a proper mesh alignment to the flow direction is essential for obtaining the asymptotic values, as is demonstrated by comparison with the results of boundary layer theory for the asymptotic case. The method presented here works in one, two and three space dimensions and is implemented for a rather general class of convection-diffusion-reaction systems [**25, 24**]. Earlier work on the numerical description of coupled transport-reaction processes in flow cells was mostly restricted to tensor product grids [**26**]. Due to unwinding, the method presented here is unconditionally stable also for high flow rates and thus is able to reproduce physical properties of the processes such as the positive value of the concentrations and the local maximum principle ("no overshoots"). Furthermore, a Levenberg-Marquardt procedure [**27**] is coupled to the solver of the partial differential equations which allows to fit model parameters to measurements.

In the present communication, we describe the transport characteristics of a novel rectangular channel flow cell design with a circular electrode by numerical simulations, and compare the model results with experimental data and with well-known asymptotic expressions. As test reaction, we use the hydrogen oxidation reaction (HOR) on a Pt/C catalyst thin-film electrode, which is an ideal example for a purely mass transport controlled electrocatalytic reaction. In contrast to the circular dual thin-layer flow cell used previously [**17**], the flow characteristics of this flow cell design is uniform. Therefore, the mathematical description of the flow pattern is much simpler compared to the pseudo-radial flow profile in the circular thin-layer flow cell, allowing the use of analytical expressions to describe the flow pattern [**28**]. The quality and relevance of the simulations is tested by comparing to experimental results for the dependence of the reaction rate on the temperature and on the electrolyte flow rate.

The paper is organized as follows: In section 2 we describe the design of the channel flow cell with a circular electrode, and present experimental results for the hydrogen oxidation reaction. In section 3 we describe the continuous model for the calculation of the limiting current, assuming Hagen Poiseuille flow of the electrolyte, and its approximation by the Voronoi box based finite volume method. In section 4 we verify the ability of this approach to resolve the parabolic boundary layer, comparing to asymptotic expressions for the limiting current at high Peclet number for the infinite strip geometry and for the circular electrode case. Finally, in section 5, we compare the numerical method with measurements described in section 2. We fit the measured data to different functional descriptions of the temperature dependence for these values. A self-contained derivation of the asymptotic expressions is provided in the appendices A and B.

2. Experimental

The experiments are performed using a novel thin-layer flow cell. The cell body is made of a chemically inert and physically resistant polymer (PolyEtherEtherKetone - PEEK). As described schematically in Fig. 1, the upper part of the flow cell consists of a glassy carbon plate ($20 \times 30 \times 5\,\mathrm{mm}^3$) with the catalyst film deposited in the middle (5 mm diameter). A glass frit placed in the polymer cell body opposite to the

$u/(\mu\mathrm{Ls}^{-1})$	$u^{1/3}/(\mu\mathrm{Ls}^{-1})^{1/3}$	i_{lim} at 20 °C	i_{lim} at 40 °C	i_{lim} at 60 °C	i_{lim} at 80 °C
0.5	0.794	0.137	0.119	0.118	0.089
1.0	1.000	0.213	0.206	0.203	0.167
2.0	1.260	0.410	0.401	0.404	0.356
5.0	1.710	0.740	0.793	0.853	0.842
10.0	2.154	1.026	1.088	1.216	1.289
20.0	2.714	1.330	1.452	1.627	1.774
50.0	3.684	1.900	2.049	2.300	2.528

TABLE 1. Table of measured values at different flow rates u and different temperatures

catalyst film separates the working electrode from the counter electrode. The flow channel is defined by a 50 µm thick polymer film gasket ($2 \times 3\,\mathrm{cm}^2$, Fluorinated Ethylene-Propylene - FEP, Bohlender) with a rectangular cut in the middle ($8 \times 12\,\mathrm{mm}^2$), which is inserted between cell body and glassy carbon plate.

The cell is ionically connected to the reference electrode (saturated calomel electrode - SCE) via a capillary at the inlet of the cell. All potentials in the paper are quoted, however, versus that of a reversible hydrogen electrode (RHE). The potential of the reference electrode was calibrated vs. the temperature by the onset of the HER/HOR in the H_2-pressurized ($3 \cdot 10^5$ Pa) supporting electrolyte. A platinum wire was used as counter electrode. Between the reference electrode and the counter electrode a capacitor (4.7 nF) had to be installed in order to slow down the feedback circuit in the potentiostat and thus prevent oscillations. In all electrochemical experiments a PINE potentiostat (model AFRDE5) was used.

The supporting electrolyte ($0.5\,\mathrm{mol} \cdot \mathrm{L}^{-1} H_2SO_4$) was prepared from Millipore MilliQ water and ultrapure sulfuric acid (Merck, suprapur). For reaction measurements, the electrolyte was first purged with Ar (99.9999% from Westfalen, Germany) to remove O_2 and then saturated with H_2 (99.999% from MTI AG, Germany), pressurized at $3 \cdot 10^5$ Pa. The exact pressure was measured by an electronic pressure meter (Wika, Tronic Line).

In order to perform experiments at elevated temperatures (40 °C, 60 °C and 80 °C), the cell was placed in a thermostated box. Thick-wall glass bottles with solutions were kept in a thermostated water bath (Lauda, EcoLine 003), and pressurized to the desired overpressure. The electrolyte flow rate was controlled by a syringe pump (Harvard Instruments, model PHD 2000) connected at the outlet of the cell.

The glassy carbon plates (Sigradur G from Hochtemperatur Werkstoffe GmbH), were polished with an alumina slurry down to 0.05 µm grade, followed by chemical etching with $5\,\mathrm{mol} \cdot \mathrm{L}^{-1}$ KOH and subsequently by concentrated H_2SO_4. After rinsing with Millipore MilliQ water, the surface was dried in a nitrogen stream. The catalyst layer (ca. 5 mm diameter) was deposited in the middle of the polished glassy carbon plate by pipetting and drying an aqueous catalyst suspension ($2\,\mathrm{mg} \cdot \mathrm{mL}^{-1}$ 20% Pt/C, E-Tek), resulting in a thin film (Pt loading $28\,\mu\mathrm{g} \cdot \mathrm{cm}^{-2}$). Finally, a thin Nafion film (thickness ca. 0.1 µm), prepared from a Nafion® solution [**29**] was used to mechanically fix the catalyst film.

The electrochemical oxidation of hydrogen was investigated measuring the anodic current at a fixed potential of 0.37 V for different flow rates u (from 0.5 to 50 $\mu\mathrm{L} \cdot \mathrm{s}^{-1}$) and different temperatures (20, 40, 60 and 80°C). The measured values of the mass transport limited current (limiting current, see below), I_{lim} at 0.37 V and different temperatures and $3 \cdot 10^5$ Pa pressure are shown in Table 1. In order to remove possible impurities adsorbed at low potential, the potential was stepped to 1.3 V after each measurement.

3. Limiting current models

3.1. Physical background. At fixed temperature T and fixed pressure p, a H_2SO_4 based electrolyte containing dissolved H_2 enters the cell at the inlet, flows over the anode, and leaves the cell at an outlet. At the inlet, the solute concentration is given by a value c_I, which depends on pressure and temperature. H_2 transported to the anode reacts at the catalytic surface according to

$$H_2 \rightarrow 2H^+ + 2e^-, \tag{3.1}$$

creating two electrons and two protons per reacted molecule. The amount of electrons generated during this reaction is measured as an electrical current. For high enough ion concentration, which is given in the present experiment ($0.5\,\mathrm{mol} \cdot \mathrm{L}^{-1}$ H_2SO_4 solution), ohmic potential drops are negligible. In a similar way, we assume that hydrogen oxidation is purely transport limited. The current measured in such a situation is called *limiting current*.

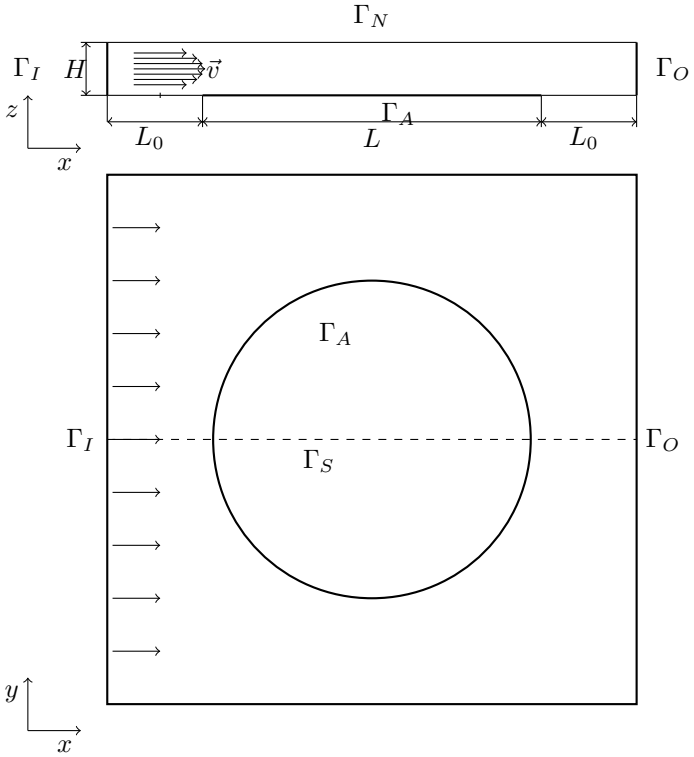

FIGURE 2. Geometry and boundary conditions of the three-dimensional cell (bottom) and its two-dimensional cross section (top)

3.2. Channel cell geometries. For the modeling of this process, we consider two idealized cell geometries, represented by two- or three-dimensional domains $\Omega \subset \mathbb{R}^d$, $d = 2, 3$. The length of the model region in the flow direction is $L + L_0$ for $d = 2$ and $L + 2L_0$ for $d = 3$.

In the first geometry, we assume a channel of height H and infinite width (see Fig. 2, top). An electrode of length L is located at the bottom of the cell. In the second geometry, a finite width of the channel and the circular geometry of the electrode are considered. The geometry, depicted in Fig. 2, represents a flow cell of width W, length L and height H. At the bottom, a circular electrode of radius R, whose center is at a distance $L_0 + R$ from the cell edge, is placed. Due to symmetry reasons, it will be sufficient to regard one half of the domain. As in the two-dimensional case, the boundary Γ of this half domain has the segments Γ_A, Γ_N, Γ_I, Γ_O. Another segment Γ_S arises at the symmetry boundary.

3.3. The continuous model. For a given velocity field $\vec{v}$ with $\nabla \cdot \vec{v} = 0$, we regard the stationary convection diffusion equation describing the concentration c of a dissolved species in a two- or three-dimensional domain,

$$-\nabla \cdot (D\nabla c - c\vec{v}) = 0. \tag{3.2}$$

Here, D is the molecular diffusion coefficient.

For the boundary $\partial\Omega = \Gamma_I \cup \Gamma_O \cup \Gamma_A \cup \Gamma_N \cup \Gamma_S$, we assume the following boundary conditions for c and conditions on $\vec{v}$:

$$\begin{array}{rcl|rcl|l}
(D\nabla c - c\vec{v}) \cdot \vec{n} & = & 0 & \vec{v} \cdot \vec{n} & = 0 & \text{on } \Gamma_S \text{ (symmetry)} \\
(D\nabla c - c\vec{v}) \cdot \vec{n} & = & 0 & \vec{v} & = 0 & \text{on } \Gamma_N \text{ (impermeable wall, no slip)} \\
(D\nabla c - c\vec{v}) \cdot \vec{n} & = & -c\vec{v} \cdot \vec{n} & & & \text{on } \Gamma_O \text{ (outflow)} \\
c & = & c_I & & & \text{on } \Gamma_I \text{ (inflow)} \\
c & = & c_A & \vec{v} & = 0 & \text{on } \Gamma_A \text{ (electrode, no slip)}
\end{array} \tag{3.3}$$

The value c_I is the inlet concentration, c_A is the boundary concentration at the anode, which in most cases will be assumed to be 0, modeling a surface reaction with infinitely fast kinetics. For reaction (3.1),

the limiting current can be calculated from the amount of solute leaving the domain at the anode as

$$I = 2F \int_{\Gamma_A} (D\nabla c - c\vec{v}) \cdot \vec{n} ds. \tag{3.4}$$

In general, $\vec{v}$ is the solution of the Navier-Stokes equations for an incompressible fluid. The velocity field in the cell geometries given in subsection 3.2 is described by the Hagen-Poiseuille law which states that the y and z components of the velocity are zero, while the x component is given by

$$v_x = 4v^\sharp \frac{z}{H}(1 - \frac{z}{H}) = 6\bar{v}\frac{z}{H}(1 - \frac{z}{H}) \tag{3.5}$$

Here, z is the vertical direction, $v^\sharp$ is the maximal flow velocity, and $\bar{v}$ is the average flow velocity. In the three-dimensional case, we use the symmetry boundary conditions at the side walls of the cell instead of the no slip boundary conditions. The assumption of symmetry boundary conditions can be justified by the fact that the width of the flow boundary layer at the side walls is small in comparison to the width of the cell [**28**]. We introduce the flow rate $u = \bar{v}WH$, where we set $W = 1$ in the two-dimensional case. Even for this simple configuration equation (3.2) has no known analytical solution. However, it can be shown that the concentration attains its maximum value at the boundaries of the domain, and that no local maxima of the concentration are found in the interior of the domain [**30**].

3.4. Asymptotic models. Due to the lack of analytical solutions, asymptotic models based on boundary layer theory have been used for a long time to derive quantitative estimates. For the channel flow with an infinite strip electrode, the solution was given in [**31**]. For the purpose of easy reference, we provide a short derivation of this estimate in appendix A. From equation (A.11), we establish the limiting current

$$I = 2FD(c_I - c_0)\frac{A}{L}Sh \tag{3.6}$$

where

$$Sh = \frac{3^{\frac{4}{3}}}{2\Gamma(\frac{1}{3})}Pe^{\frac{1}{3}} \approx 0.8075491 Pe^{\frac{1}{3}} \tag{3.7}$$

is the dimensionless Sherwood number, and A is the electrode surface, which in this case is equal to L. The dimensionless Peclet number Pe is defined by $Pe = \frac{\beta L^2}{D}$, where $\beta = \frac{6\bar{v}}{H}$.

For the case of a circular electrode, an asymptotic estimate has been mentioned by [**32**]. The derivation, presented in appendix B for $Pe = \frac{\beta R^2}{D}$ [**32, 33**], yields

$$I = 2FD(c_I - c_0)\pi R Sh \tag{3.8}$$

with

$$Sh = \frac{3^{\frac{4}{3}}2^{\frac{2}{3}}}{5\sqrt{\pi}\Gamma(\frac{5}{6})}Pe^{\frac{1}{3}} = \frac{2^{\frac{1}{3}}3^{\frac{4}{3}}\Gamma(\frac{1}{3})}{5\pi\Gamma(\frac{2}{3})}Pe^{\frac{1}{3}} \approx 0.68658 Pe^{\frac{1}{3}}. \tag{3.9}$$

The second expression can be found in [**32, 33**].

3.5. Finite volume models. Numerical models have the potential to avoid the limitations of asymptotic models. Furthermore, they can be generalized to more complex processes. They are derived from continuous models like (3.2) by discretization. A particular discretization method is the Voronoï box based finite volume method [**34**], known also as "box method" [**35**] or "control volume method".

This discretization is based on a subdivision of the domain Ω (see 3.3) into a finite number of open, polygonal control volumes K around the discretization points $\vec{x}_K$. Such a control volume subdivision can be obtained by using a triangular or tetrahedral grid. For this grid, we require the boundary-conforming Delaunay property [**36**]. This means that for any given triangle resp. tetrahedron (simplex) of the grid, the interior of the circle resp. ball spanned by its vertices does not contain any vertex of any other simplex, and that its center is located in the interior of the domain Ω or its boundary. In two space dimensions, the mesh generator "triangle" [**37**] is able to create this type of grids. In three space dimension, this question is still under research. With a 70^o constraint on the input angles, TetGen [**38**] allows to create this type of meshes.

This Delaunay property allows to obtain the control volumes surrounding each given discretization node by joining the circumcenters of the simplices adjacent to it (Fig. 3).

By ∂K, we denote the boundary of the control volume K, and by $|\xi|$, the measure (volume, surface, length) of a geometrical object ξ. For each control volume K, we integrate equation (3.2) and apply the

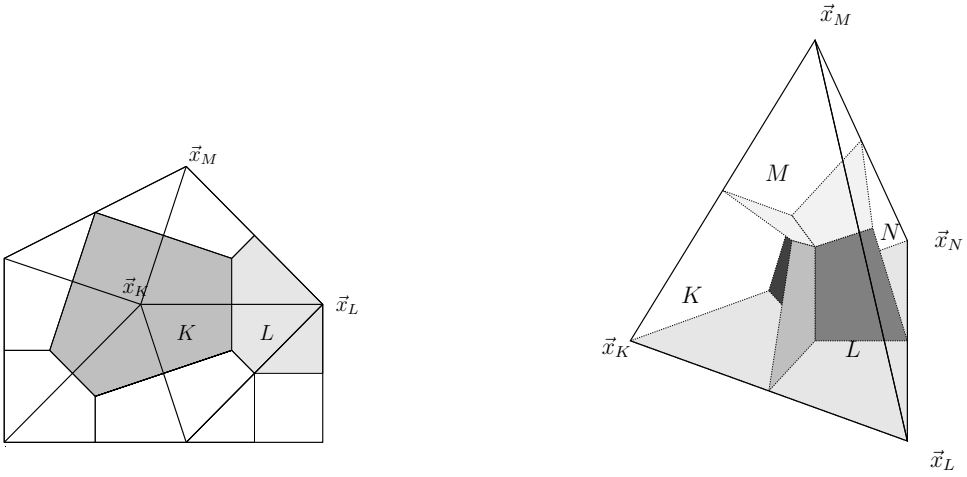

FIGURE 3. Simplices and control volumes in two and three space dimensions

Gauss theorem to the integral of the flux divergence. After that, we choose appropriate approximations for the remaining integrals:

$$
\begin{aligned}
0 &= -\int_K \nabla\cdot(D\nabla c - c\vec{v})dx = -\int_{\partial K}(D\nabla c - c\vec{v})\cdot\vec{n}ds \\
&= -\sum_{L \text{ neighbor of } K}\int_{\partial K\cap\partial L}(D\nabla c - c\vec{v})\cdot\vec{n}_{KL}ds - \sum_{\sigma\in\Gamma\cap\partial K}\int_\sigma (D\nabla c - c\vec{v})\cdot\vec{n}_\sigma ds \\
&\approx \sum_{L \text{ neighbor of } K}\frac{|\partial K\cap\partial L|}{|\vec{x}_K - \vec{x}_L|}g(c_K, c_L, v_{KL}) \quad \text{main part} \\
&\quad + \sum_{\sigma\in\Gamma_N\cap\partial K}|\sigma|0 \quad \text{no flux} \\
&\quad + \sum_{\sigma\in\Gamma_O\cap\partial K}|\sigma|g(c_K, c_K, v_\sigma) \quad \text{outflow} \\
&\quad + \sum_{\sigma\in\Gamma_I\cap\partial K}\frac{1}{\varepsilon}(c_K - c_I) + \sum_{\sigma\in\Gamma_A\cap\partial K}\frac{1}{\varepsilon}(c_K - c_0) \quad \text{inflow, anode}
\end{aligned}
\tag{3.10}
$$

Here, c_K is the average value of the unknown in the control volume. For any planar facet $\sigma \subset \bar{\Omega}$,

$$
v_\sigma = \frac{1}{|\sigma|}\int_\sigma \vec{v}\cdot\vec{n}ds \tag{3.11}
$$

is the average normal flux of $\vec{v}$ through σ. The flux function $g(c_K, c_L, v_{KL})$ is an approximation of the scaled normal flux $(-D\nabla c + c\vec{v})\cdot(\vec{x}_K - \vec{x}_L)$ through the facet $\partial K \cap \partial L$. The summation goes over all planar facets belonging to ∂K. These may be interfaces to neighboring control volumes, or parts of the boundary $\partial\Omega$. Expressions for the flux function can be derived from one-dimensional upwind finite difference approximations. In our discrete model, we define the flux function by

$$
g(c_K, c_L, v) = D\left(U\left(\frac{v}{D}\right)c_K - U\left(-\frac{v}{D}\right)c_L\right), \tag{3.12}
$$

where $U(\xi)$ is an upwind function [**39**]. A preferable choice for the function U, which goes back to Allen and Southwell [**40**], is

$$
U(\xi) = B(\xi) = \frac{\xi}{e^\xi - 1}. \tag{3.13}
$$

This choice, also known as exponential fitting scheme, keeps the amount of artificial diffusion added for the purpose of stabilization low by utilizing the diffusion inherent to the problem. It can be derived from a solution of a projection of the transport problem (3.2) onto the one-dimensional edge $\vec{x}_K\vec{x}_L$. The validity of the expression from the outflow boundary condition follows from the particular property $g(c, c, v) = cv$. The Dirichlet boundary conditions are implemented by a penalty method which for

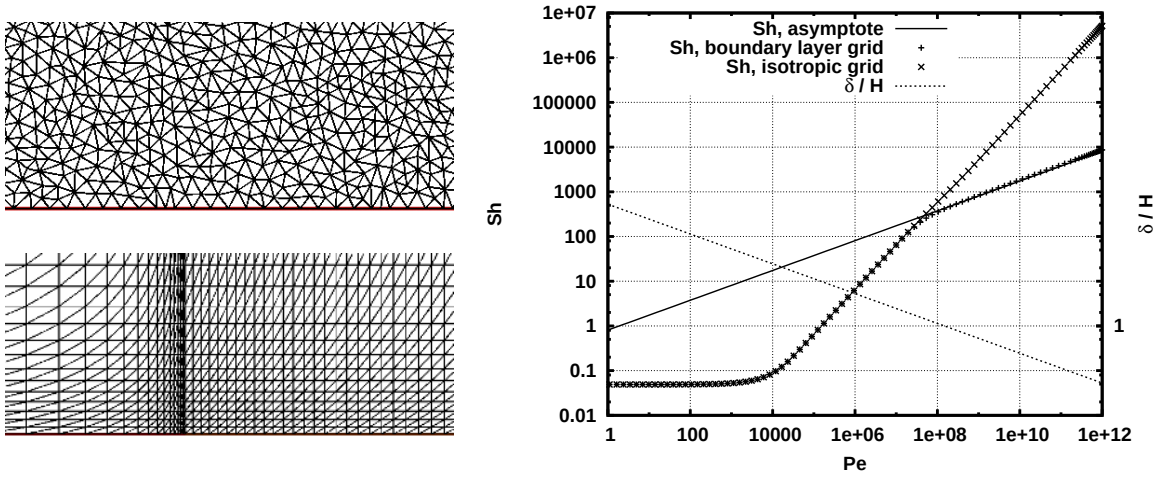

FIGURE 4. Sh vs. Pe and $\frac{\delta}{H}$ vs. Pe for 2D case. Left: Detail of the isotropic triangular and adapted aligned meshes. Right: Plots of Leveque asymptote, Sh vs. Pe and relative boundary layer thickness vs. Pe

$\varepsilon << 1$ in the corresponding nodes leads to $c_K = c_I$ resp. $c_K = c_A$ in the floating point arithmetic of the computer.

For the calculation of boundary fluxes, we use a scheme which is similar to that used in [**41**]. For the motivation, we start with the continuous case. Assume that the boundary $\partial\Omega = \Gamma = \Gamma_N \bigcup (\bigcup_i \Gamma_i)$ is subdivided into non-overlapping boundary parts such that $\vec{v}(x) \cdot \vec{n} = 0$ and $(D\nabla c - c\vec{v}) \cdot \vec{n} = 0$ on Γ_N. Let T be a test function such that $\nabla T \cdot \vec{n} = 0 \quad \text{on} \quad \Gamma_N$, $T|_{\Gamma_i} = 1$ and $T|_{\Gamma_j} = 0$ for $j \neq i$. To obtain the flux Q through the boundary piece Γ_i, we calculate, using $\nabla \cdot \vec{q} = 0$:

$$Q = \int_{\Gamma_i} T\vec{q} \cdot \vec{n} d\gamma + \int_{\Gamma_N} T\vec{q} \cdot \vec{n} d\gamma + \sum_{l \neq i} \int_{\Gamma_l} T\vec{q} \cdot \vec{n} d\gamma \tag{3.14}$$

$$= \int_{\Gamma} T\vec{q} \cdot \vec{n} d\gamma = \int_{\Omega} \nabla \cdot (T\vec{q}) d\omega = \int_{\Omega} \nabla T \cdot \vec{q} d\omega \tag{3.15}$$

The last term is discretized in the following way,

$$Q = \int_{\Omega} \nabla T \cdot \vec{q} d\omega \approx \sum_{\substack{K,L \\ \partial K \cup \partial L \neq \emptyset}} (\nabla T)_{KL}\, q_{KL}\, a_{KL} \quad = \sum_{\substack{K,L \\ \partial K \cup \partial L \neq \emptyset}} \frac{|\partial K \cup \partial L|}{|\vec{x}_K - \vec{x}_L|} (T_K - T_L) g(c_K, c_L) \tag{3.16}$$

Here, $a_{KL} = \frac{1}{d}|\partial K \cup \partial L||\vec{x}_K - \vec{x}_L|$ is the volume of the "diamond", the double pyramid spanned by the interface $\partial K \cup \partial L$ between two control volumes and the end points of the corresponding edge $\vec{x}_K, \vec{x}_L$. The discrete gradient writes as $(\nabla T)_{KL} = d\frac{T_K - T_L}{|\vec{x}_K - \vec{x}_L|}$, and the flux projection is by the very definition of the finite volume scheme $q_{KL} = g(c_K, c_L, v_{KL})$.

The described discretization results in linear systems of equations with sparse matrices. For the solution we use the solver Pardiso[**42**], which as a direct solver with an efficient storage scheme.

4. Comparison between finite volume and asymptotic models

4.1. Limiting current asymptotics in for a 2D problem ("infinite strip case"). The geometry of the two-dimensional problem is depicted on the top in Fig. 2. The measures of the cell are $H = 50\,\mu\text{m}$, $L_0 = 1\,\text{mm}$, $L = 9\,\text{mm}$. Furthermore, we set $c_I = 1\,\text{mol}\cdot\text{m}^{-3}$, $D = 9.5 \cdot 10^{-9}\,\text{m}^2 \cdot \text{s}^{-1}$. In this case, equation (A.11) yields a mass transfer rate $M = 0.055362 \left(\frac{v^\sharp}{HD}\right)^{\frac{1}{3}}\,\text{mol}\cdot\text{s}^{-1}$. We performed calculations for $Pe = \frac{4L^2}{HD} v^\sharp$ varying from 1 to 10^{12} with an isotropic triangular grid with 204682 vertices (created by "triangle" [**37**]), and with another grid aligned with the flow direction and adapted to the boundary layer and the electrode edge, with 64000 vertices, as shown in Fig. 4, left. In Fig. 4, right, we see that the finite volume solution properly describes the asymptotic behavior of the Sherwood number for a wide range of Peclet numbers, provided, the grid is aligned to the flow and the boundary layer is resolved. The asymptotic regime is reached on the boundary layer grid for $Pe \gtrapprox 10^8$. From equation

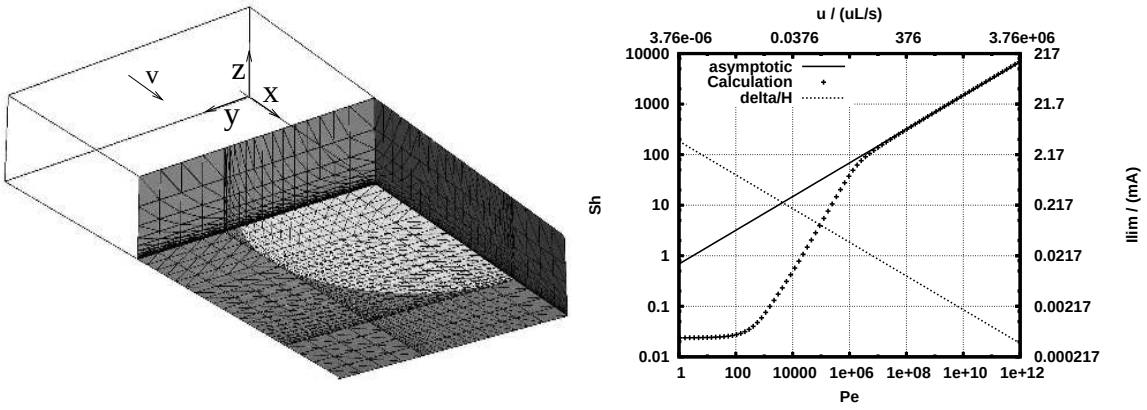

FIGURE 5. Sh vs. Pe and $\frac{\delta}{H}$ vs. Pe for 3D case. Left: Detail of flow-aligned 3D grid. Right: Plots of Leveque asymptote, Sh vs. Pe: asymptotic curve and numerical result for the 3D model with circular electrode.

$T/°\mathrm{C}$	$D/(10^{-9}\ \mathrm{m}^2\cdot\mathrm{s}^{-1})$	$k_H/(10^{-2})$	$c_I/(\mathrm{mol}\cdot\mathrm{m}^{-3})$
20	3.2	1.95	2.40
40	4.9	1.85	2.13
60	7.1	1.86	2.01

TABLE 2. Literature values from[**44**] of the diffusion coefficient D, the Henry constant k_H for $p = 10^5$ Pa and the resulting c_I value, from Henry's law for $p = 3\cdot 10^5$ Pa.

(A.16), for the maximal thickness of the boundary layer, we get $\delta \approx 2.932 L Pe^{-\frac{1}{3}}$. In Fig. 4, we additionally plotted the value of $\frac{\delta}{H}$ vs. the Peclet number. The transition to the asymptotic regime is clearly correlated with $\frac{\delta}{H} < 1$. The isotropic grid is unable to approximate the asymptotic behavior of the Sherwood number, though it contains six times more nodes than the aligned grid.

The above observations agree with theoretical findings concerning numerical methods for problems with diffusive boundary layers [**43**].

4.2. Limiting current asymptotics for a 3D problem ("Circular electrode case"). In the case of a circular electrode, it is not possible to reduce the calculations to a two-dimensional cross-section. We have to solve a three-dimensional problem.

Based on the experience from the two-dimensional case, we constructed grids which are aligned with the flow direction and have exponentially decreasing distances of grid lines towards the catalyst boundary, and at the same time are able to reflect the circular electrode geometry, as illustrated in Fig. 5, left. Grids of this type with three consecutive refinement levels and 1080, 6426, and 43758 nodes, respectively will be used in the next section.

The simulation results for Peclet numbers varying from 1 to 10^{12} are plotted in Fig. 5, right, in order to compare them to the asymptotic estimate (3.9). The numerical method is able to describe the asymptotic behavior sufficiently well. For the given geometry, the transition from the diffusion limited regime (small Pe) to asymptotic behavior (large Pe) takes place for $Pe \approx 10^7$.

5. Comparison between finite volume model and experiment

In this section, we compare our numerical model to the experimental data measured as described in section 2. For the geometry given above and assuming infinitely fast kinetics, there are three parameters: the flow rate, which is fixed by the experimental conditions, the inlet concentration c_I and the molecular diffusion coefficient D. In a first model run, we use literature values and perform no fitting, while in further model runs, we use fitting for various approaches concerning D and c_I.

5.1. Simulation with literature values for D and c_I. In a first approach, we model the experimental set-up using the literature values [**44**] for the parameters D and c_I, which are listed in table 2. The diffusion coefficient increases with temperature, and the inlet concentration decreases with temperature.

The limiting currents, obtained for different temperatures, are plotted as a function of the electrolyte flow rate in Fig. 6. The experimentally determined and calculated limiting currents have the same order of magnitude. Both experimental and simulated values decrease with temperature at low flow rates, and

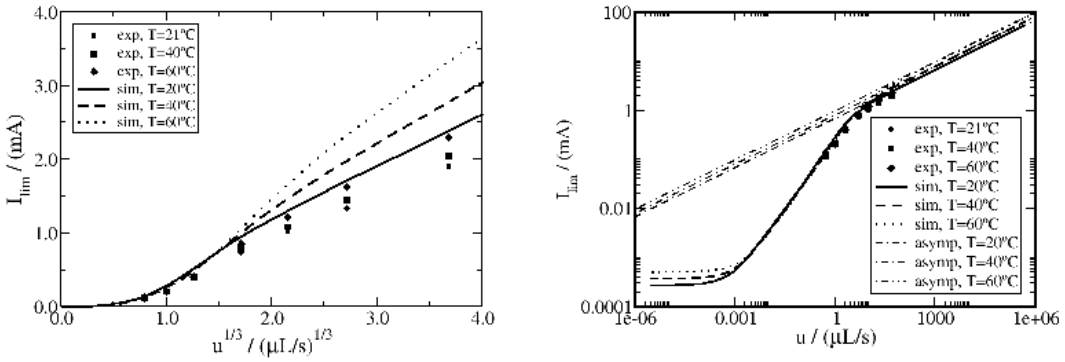

FIGURE 6. Experimentally determined and simulated limiting HOR currents, using values for D and c_I from [**44**] (table 2). Current vs. third root of flow rate – left. Comparison to the asymptotic current vs. flow rate behavior

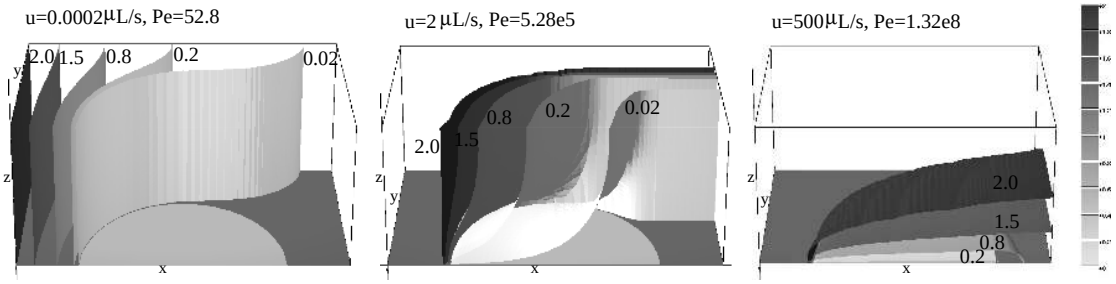

FIGURE 7. Concentration iso-surfaces at different Peclet numbers for the half cell at 40°C. The circular electrode is located at the bottom.

increase at high flow rates. This leads to a crossing of the low and high temperature curves at a flow rate between 2 and 5 $\mu L \cdot s^{-1}$. This crossing agrees with the experimental observation.

The log-log plot in Fig. 6, right, reveals that at the lower flow rates applied in the experiment, the cell works in the sub-asymptotic regime, i.e. the observed boundary layer is thicker than the cell height. Consequently, the limiting current scales with "$u^{\frac{1}{3}}$" only for higher flow rates u. In Fig. 7, surfaces of constant concentration are plotted. For the experiments described above, the assumption of working in the asymptotic regime is true for the higher flow rates.

At the same time, we observe that the simulated values are slightly larger than those measured. As we could attribute the uncertainty of the data for c_I and D as one reason for this fact, in the sequel, we fit these data to our measurements.

5.2. Independent fit for D and c_I at each temperature. We fit the two open parameters D and c_I individually for each temperature, resulting in the values provided in table 4. The fit results are visualized in the top row of Fig. 8. Except for the 80°C curve for lower flow rates, we get a very good agreement between measured and fitted data.

The fitted values for D are in the range of magnitude usually found in the literature. Furthermore, we observe a monotonic increase of D with temperature, and a decrease of c_I with temperature.

5.3. Fit of D and c_I for temperature dependent models. We examine a more general approach utilizing temperature dependent models for D and c_I. As a general model for the diffusion coefficient, we assume [**45**]

$$D(T) = D_0 \exp\left(-\frac{k_D}{RT}\right) \tag{5.1}$$

For the inlet concentration, we assume equilibrium according to Henry's law in the following form [**44**]:

$$c = \frac{k_H}{RT} p \tag{5.2}$$

where the Henry constant k_H is dimensionless.

n_{ref}	2	3	4
	Model (5.1), (5.2), (5.3) ($k_H = \text{const}$)		
$D_0/(10^{-7}\,\text{m}^2\cdot\text{s}^{-1})$	2.6634	2.8579	2.9519
$k_D/(10^4\,\text{J}\cdot\text{mol}^{-1})$	1.1269	1.1192	1.1173
$k_H/(10^{-2})$	1.5281	1.5583	1.5642
	Model (5.1), (5.2), (5.4) ($k_H = k_0 \exp(-\frac{k_c}{RT})$)		
$D_0/(10^{-7}\,\text{m}^2\cdot\text{s}^{-1})$	2.2531	2.3440	2.4242
$k_D/(10^4\,\text{J}\cdot\text{mol}^{-1})$	1.0809	1.0647	1.0631
$k_0/(10^{-2})$	1.6901	1.7574	1.7630
$k_c/(10^2\,\text{J}\cdot\text{mol}^{-1})$	2.7760	3.3126	3.2941
	Model (5.1), (5.2), (5.5) ($k_H = k_0 RT \exp(-\frac{k_c}{RT})$)		
$D_0/(10^{-8}\,\text{m}^2\cdot\text{s}^{-1})$	4.9832	5.4481	5.8973
$k_D/(10^3\,\text{J}\cdot\text{mol}^{-1})$	6.6958	6.6628	6.7536
$k_1/(10^{-6}\,\text{mol}\cdot\text{J}^{-1})$	5.5781	5.6831	5.6846
$k_1 RT_{ref}/(10^{-2})$	1.5451	1.5742	1.5746
$k_c/(10^{-5}\,\text{J}\cdot\text{mol}^{-1})$	1.9937	2.2155	2.2814

TABLE 3. Constants for various models for temperature dependent inlet concentrations and diffusion coefficients on three grid levels in the temperature range 21 - 80°C. In order to verify that $k_1 RT$ in model (5.5) has the same order as k_0 in model (5.4), $k_1 RT_{ref}$ is calculated, where $T_{ref} = 60°\text{C}$.

The expression for the temperature dependence of the Henry constant k_H is discussed controversially in the literature. Following different proposals found in the literature, we assume a constant value

$$k_H = \text{const}, \tag{5.3}$$

or alternatively [**46**]

$$k_H = k_0 \exp(-\frac{k_c}{RT}), \tag{5.4}$$

or

$$k_H = k_1 RT \exp(-\frac{k_c}{RT}). \tag{5.5}$$

By inverse modeling, we estimate parameters for all three approaches. Table 3 lists the fit parameters for each approach in the first column. In order to fit these values, we couple the code levmar [**27**] for parameter identification based on the Levenberg-Marquardt method to our software. The results for the fits to the three models are presented in table 3. The resulting values for the diffusion coefficients and inlet concentrations are shown in table 4, together with those for the individual fit. In table 5, we present the corresponding values for the least squares functionals. Each of the described models is fitted on the three different grids described in subsection 4.2. Plots of limiting current in dependence of $u^{1/3}$ for experimental and numerical output are given in 8. These plots are based on the finest grid only.

We judge the quality of the fit by the resulting values of the least squares functional from table 5, which should be as small as possible. As a general rule, the fit quality improves with finer grids. The best value is attained by the individual fit for each temperature, as could be expected. In this case, we present the sum of the values for the least squares functionals for the individual fits.

The second best fit was obtained with exponential formula for the Henry constant (5.4), closely followed by the model with constant k_H (5.3). The more complex approach for k_H (5.5) is significantly worse. This is clearly visible in Fig. 8 (d), where the inversion of the monotonicity behavior of the current with respect to temperature at a flow rate of approximately $(1.4)^3\ \mu\text{L}\cdot\text{s}^{-1}$ is not observed in the simulated curves.

5.4. Discussion. Diffusivity values obtained in section 5.2 and 5.3 agree well to those found in the literature. For the Henry constant, resp. inlet concentration, we obtain slightly lower values compared to those in the literature. One has to be aware, however, that we did not find any directly measured values for $p = 3 \cdot 10^5$ Pa to compare with.

There may be different reasons for the lower inlet concentrations compared to those from the literature. Our assumption that the process of hydrogen dissolution is in equilibrium may not be fully justified. The same holds true for the assumption of an infinitely fast reaction.

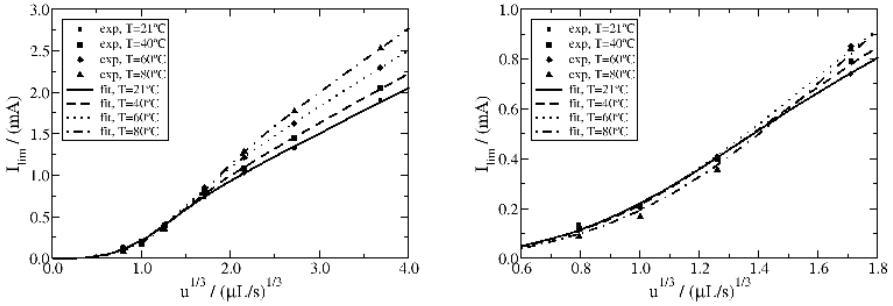

(a) Individual fit for different temperature curves

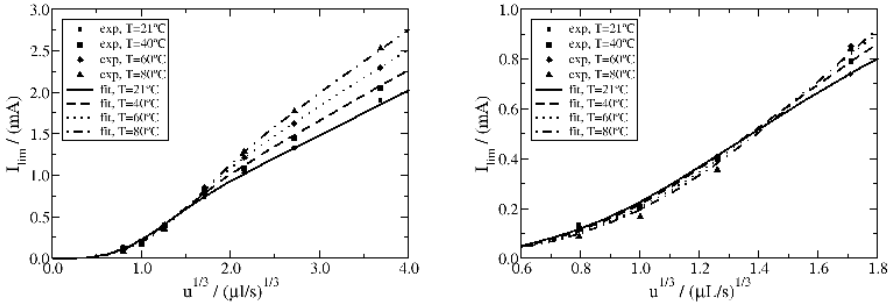

(b) Model (5.1), (5.2), (5.3) ($k_H = \text{const}$)

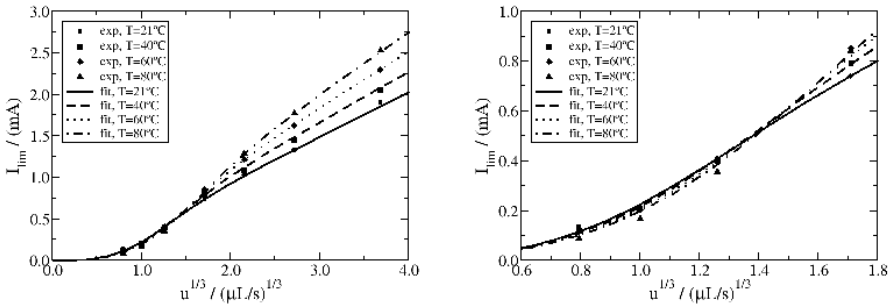

(c) Model (5.1), (5.2), (5.4) ($k_H = k_0 \exp(-\frac{k_c}{RT})$)

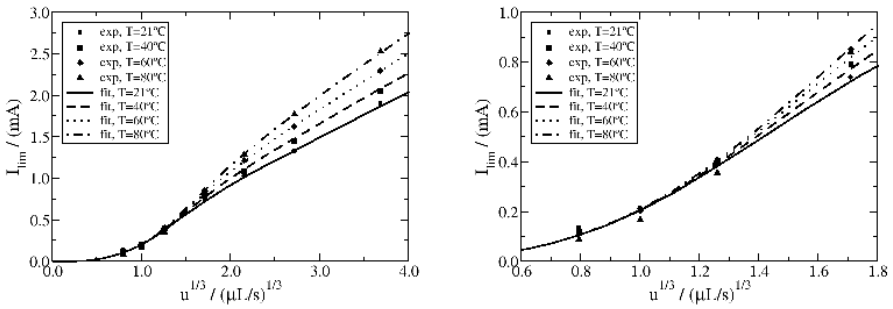

(d) Model (5.1), (5.2), (5.5) ($k_H = k_0 RT \exp(-\frac{k_c}{RT})$)

FIGURE 8. Fits of the calculated limiting currents to measured values as a function of flow rate using different models on the finest grid with $n_{\text{ref}} = 4$.

6. Summary and outlook

In this paper, we presented results of a combined experimental and numerical study on the transport characteristics of a flow cell with rectangular geometry and circular electrode, which was designed for

	$D/(10^{-9}\,\mathrm{m}^2\cdot\mathrm{s}^{-1})$			$c_I/(\mathrm{mol}\cdot\mathrm{m}^{-3})$			$(c_I/p)/(10^{-5}\,\mathrm{mol}\cdot\mathrm{m}^{-3}\cdot\mathrm{Pa}^{-1})$		
n_{ref}	2	3	4	2	3	4	2	3	4
$T/°\mathrm{C}$	Individual fit for different temperature curves								
21	2.8679	3.1905	3.3221	1.8141	1.8439	1.8508	0.6047	0.6146	0.6169
40	3.4429	3.8207	3.9766	1.7499	1.7803	1.7871	0.5833	0.5934	0.5957
60	4.1895	4.6315	4.8204	1.7390	1.7719	1.7784	0.5797	0.5906	0.5928
80	6.0014	6.5819	6.8405	1.5289	1.5626	1.5689	0.5096	0.5209	0.5230
	Model (5.1), (5.2), (5.3) ($k_H = \mathrm{const}$)								
21	2.6568	2.9415	3.0629	1.8744	1.9115	1.9187	0.6248	0.6372	0.6396
40	3.5138	3.8829	4.0412	1.7607	1.7955	1.8023	0.5869	0.5985	0.6008
60	4.5563	5.0261	5.2287	1.6550	1.6877	1.6941	0.5517	0.5626	0.5647
80	5.7369	6.3184	6.5704	1.5612	1.5921	1.5982	0.5204	0.5307	0.5327
	Model (5.1), (5.2), (5.4) ($k_H = k_0 \exp(-\frac{k_c}{RT})$)								
21	2.7129	3.0154	3.1394	1.8507	1.8827	1.8900	0.6169	0.6276	0.6300
40	3.5473	3.9269	4.0867	1.7504	1.7830	1.7899	0.5835	0.5943	0.5966
60	4.5512	5.0196	5.2219	1.6559	1.6888	1.6953	0.5520	0.5629	0.5651
80	5.6768	6.2403	6.4896	1.5710	1.6040	1.6101	0.5237	0.5347	0.5367
	Model (5.1), (5.2), (5.5) ($k_H = k_0 RT \exp(-\frac{k_c}{RT})$)								
21	3.2248	3.5735	3.7272	1.6734	1.7049	1.7054	0.5578	0.5683	0.5685
40	3.8076	4.2158	4.4070	1.6734	1.7049	1.7054	0.5578	0.5683	0.5685
60	4.4432	4.9159	5.1496	1.6734	1.7049	1.7054	0.5578	0.5683	0.5685
80	5.0950	5.6333	5.9120	1.6734	1.7049	1.7054	0.5578	0.5683	0.5685

TABLE 4. Diffusion coefficient and inlet concentrations for $0.5\,\mathrm{mol}\cdot\mathrm{L}^{-1}$ H_2SO_4 at $p = 3\cdot10^5$ Pa (rounded to five significant digits) resulting from fits for different models on three grid levels

n_{ref}	2	3	4
Ind. fit	0.006182	0.004795	0.004256
(5.1), (5.2), (5.3)	0.01187	0.01045	0.009914
(5.1), (5.2), (5.4)	0.01182	0.01037	0.009839
(5.1), (5.2), (5.5)	0.01497	0.01345	0.01288

TABLE 5. Values of least squares functional for the fits for the different models on three grid levels.

kinetic measurements in electrocatalytic reactions. As test reaction, we used H_2 oxidation on a thin-layer carbon supported Pt catalyst electrode, which at overpotentials $> 50\,\mathrm{mV}$ can be assumed to be infinitely fast. The corresponding model is based on the transport equation with zero homogeneous Dirichlet boundary conditions (zero concentration) at the anode, which is classically used for deriving the asymptotic behavior valid at high flow rates. A numerical model, based on the finite volume method, is introduced, which allows a proper description of the transport properties in the cell under both slow and fast flow conditions. It is verified to predict the correct behavior for the asymptotic case and applied to describe the temperature dependent transport behavior for more general temperature dependent set-ups.

Comparison between asymptotic models and the finite volume based numerical model reveals that proper grid alignment is essential for correct asymptotic results. Properly aligned grids are constructed which yield the correct asymptotic behavior for flow rates orders of magnitude larger than those used in experiments. Second, using literature values for the model parameters (H_2 diffusion coefficient, inlet concentration of hydrogen) in the numerical model, we compared the numerical data with experimental results and find good agreement in the qualitative features, but slightly higher anodic currents in the numerical model than those measured. Furthermore, this comparison reveals that in the measured range of flow rates, the cell operates in the transition regime between diffusive (low flow rates) and the asymptotic behavior obtained at higher flow rates. As a consequence, we fit the model parameters to the measurements. Fitting these parameters by comparison of calculated and experimentally determined limiting currents leads to good agreement for temperature dependent parameters, described by an exponential law for the diffusion coefficient (model (5.1)) and a constant value of the Henry constant (model (5.2) and (5.3)). The established values of the diffusion coefficient agree with those reported in the literature,

while the resulting inlet concentrations are slightly lower than those found in the literature. This was tentatively attributed to a loss of H_2 e.g. on the way from the supply bottle to the reaction cell or remaining kinetic limitations.

The paper clearly demonstrates that the chosen numerical modeling approach properly describes both the transport behavior derived from asymptotic theory and the experimental data. It is applicable also for transport conditions which are not covered by the asymptotic theory, e.g., if the boundary layer thickness exceeds the cell height. It thus allows the experimentalist to quickly decide whether the experiments are performed under conditions where asymptotic theories can be applied. For the future, we plan to extend this numerical model by including the reaction kinetics and to apply the combined modeling and experimental approach to study the kinetics of electrocatalytic reactions where both reaction kinetics and transport contribute to the measured Faradaic current and hence to the overall reaction rate. Another direction of generalization is the inclusion of other cell geometries, which involves the numerical solution of the Navier-Stokes equations, and a mass-conservative coupling to the numerical scheme for the transport equation described in the present paper.

7. Acknowledgments

We acknowledge the support of this work by the German Federal Ministry of Education and Research, grant Nos. 03SF0311A and 03SF0311C.

Appendix A. Estimates of limiting current asymptotics for an infinite strip

For the purpose of easy reference, we derive the mass transfer estimate for the asymptotic of high Peclet numbers. In appendix A, we deal with the idealized case of an electrode with finite length in flow direction, while appendix B concerns a circular electrode. In the first case, the constellation allows a 2D description.

The boundary layer theory for a constant shear rate case is due to Leveque [**31**]. Our derivation follows that in ref. [**47**] (see also references cited therein). We consider the problem (3.2) in the two-dimensional cross-section of an infinite strip described in Fig. 2 (top). Throughout the appendix, the coordinate direction orthogonal to the electrode surface will be denoted by y instead of z.

A Taylor expansion allows to express the flow velocity near $y = 0$ using the shear rate β and its derivative:

$$v_x = y\beta(x), v_y = -\frac{1}{2}y^2\beta'(x). \tag{A.1}$$

Close to the boundary, $\frac{\partial^2 c}{\partial x^2}$ is neglected, leading to the boundary layer equation

$$-D\frac{\partial^2 c}{\partial y^2} + y\beta\frac{\partial c}{\partial x} - \frac{1}{2}y^2\beta' = 0. \tag{A.2}$$

Defining the similarity variable

$$\xi = \frac{y\sqrt{\beta}}{(9D\int_0^x \sqrt{\beta}dx)^{\frac{1}{3}}} \tag{A.3}$$

and setting $c = c(\xi)$, a straightforward calculation gives

$$\frac{\partial c}{\partial y} = c'\frac{\xi}{y}, \qquad \frac{\partial^2 c}{\partial y^2} = c''\frac{\xi^2}{y^2}, \qquad \frac{\partial c}{\partial x} = c'\frac{\xi\beta'}{2\beta} - c'\frac{3D\xi^4}{y^3\beta}. \tag{A.4}$$

Using this ansatz, equation (A.2) becomes

$$c'' - 3\xi^2 c' = 0. \tag{A.5}$$

It has the general solution

$$c(\xi) = \mathcal{C}_0 + \mathcal{C}_1\int_0^\xi e^{-x^3}\ dx. \tag{A.6}$$

Setting the boundary conditions $c(0) = c_0$ and $c(\infty) = c_I$, we can express

$$c(\xi) = c_0 + (c_I - c_0)\frac{\int_0^\xi e^{-x^3}dx}{\int_0^\infty e^{-x^3}dx} = c_0 + (c_I - c_0)\frac{\gamma(\frac{1}{3},\xi^3)}{\Gamma(\frac{1}{3})}.$$

Here, we use

$$\int_0^\xi e^{-x^3}dx = \frac{1}{3}\int_0^{\xi^3} t^{\frac{1}{3}-1}e^{-t}\ dt = \frac{1}{3}\gamma(\frac{1}{3},\xi^3). \tag{A.7}$$

$\Gamma(a)$ is the gamma function, and $\gamma(a,x)$ is the incomplete gamma function [**48**]. Note that this function is linear in the vicinity of $\xi = 0$ with

$$c'(0) = \frac{(c_I - c_0)}{\Gamma(\frac{4}{3})} \tag{A.8}$$

due to the recurrence equation $\Gamma(a+1) = a\Gamma(a)$. Therefore, the mass transfer rate through the electrode boundary can be calculated as

$$M(x) = D\frac{\partial c}{\partial y}|_{y=0} = Dc'(0)\frac{\sqrt{\beta}}{(9D\int_0^x \sqrt{\beta}dx)^{\frac{1}{3}}} = D\frac{(c_I - c_0)}{\Gamma(\frac{4}{3})}\frac{\sqrt{\beta}}{(9D\int_0^x \sqrt{\beta}dx)^{\frac{1}{3}}}. \tag{A.9}$$

For a constant value of β we obtain

$$M(x) = D\frac{(c_I - c_0)}{\Gamma(\frac{4}{3})}\left(\frac{\beta}{9Dx}\right)^{\frac{1}{3}}. \tag{A.10}$$

Integrating over electrode length L, and introducing the dimensionless Peclet number $Pe = \frac{\beta L^2}{D}$, we can express M_L as [**33**]

$$M_L = D(c_I - c_0)\frac{3^{\frac{1}{3}}}{2\Gamma(\frac{4}{3})}\left(\frac{\beta L^2}{D}\right)^{\frac{1}{3}} = D(c_I - c_0)\frac{A}{L}Sh, \tag{A.11}$$

where

$$Sh = \frac{3^{\frac{4}{3}}}{2\Gamma(\frac{1}{3})}Pe^{\frac{1}{3}} \approx 0.8075491Pe^{\frac{1}{3}} \tag{A.12}$$

is the dimensionless Sherwood number and A is the electrode surface, which in this case is equal to L.

In the case of Hagen-Poiseuille flow, we get $\beta = 6\frac{\bar{v}}{H} = 4\frac{v^\sharp}{H}$. Therefore, using the estimate $\Gamma(\frac{4}{3}) = 0.8929795$ [**49**], we arrive at

$$M(x) = D\frac{(c_I - c_0)}{\Gamma(\frac{4}{3})}\left(\frac{2\bar{v}}{3HDx}\right)^{\frac{1}{3}} \approx 0.97827D(c_I - c_0)\left(\frac{\bar{v}}{HDx}\right)^{\frac{1}{3}}, \tag{A.13}$$

see also [**47**].

The thickness δ of the boundary layer can be derived in the following way. ξ^* is defined such that $c(\xi^*) = (1-\varepsilon)c_I$. From the definition of the similarity variable (A.3) in the case of constant $\beta = \frac{6\bar{v}}{H}$ we obtain

$$\xi^* = \delta\left(\frac{\beta}{9Dx}\right)^{\frac{1}{3}} \quad \text{and} \quad \delta = \xi^*\left(\frac{9Dx}{\beta}\right)^{\frac{1}{3}}. \tag{A.14}$$

Setting $\varepsilon = 0.01$, we estimate [**49**] that $\xi^* \approx 1.41$. Therefore,

$$\delta \approx 2.932\left(\frac{Dx}{\beta}\right)^{\frac{1}{3}}, \tag{A.15}$$

and the maximal thickness of the boundary layer can be estimated as

$$\delta^\sharp \approx= 2.932LPe^{-\frac{1}{3}}. \tag{A.16}$$

Appendix B. Limiting current asymptotic for a circular electrode

The case of a circular electrode constitutes a 3D problem, that cannot be reduced to 2D. Ignoring lateral diffusion, we attempt to calculate the limiting current for a circular electrode by integrating equation (A.11) over the electrode domain, using $L = L(y) = 2(R^2 - y^2)^{\frac{1}{2}}$ and (A.11), this results in

$$M_R = D(c_I - c_0)\frac{3^{\frac{1}{3}}}{2^{\frac{1}{3}}\Gamma(\frac{4}{3})}\left(\frac{\beta}{D}\right)^{\frac{1}{3}}\int_{-R}^{R}(R^2 - y^2)^{\frac{1}{3}}dy. \tag{B.1}$$

According to mathematica [**50**], using the Gauss hypergeometric function ${}_2F_1$ [**48**], the indefinite integral is expressed as

$$\int (R^2 - y^2)^{\frac{1}{3}}dy = \frac{3R^2y - 3y^3 + 2R^2y(1 - \frac{y^2}{R^2})^{\frac{2}{3}}\ {}_2F_1(\frac{1}{2}, \frac{2}{3}, \frac{3}{2}; \frac{y^2}{R^2})}{5(R^2 - y^2)^{\frac{2}{3}}} \tag{B.2}$$

$$= \frac{3}{5}y(R^2 - y^2)^{\frac{1}{3}} + \frac{2}{5}yR^{\frac{2}{3}}\ {}_2F_1(\frac{1}{2}, \frac{2}{3}, \frac{3}{2}; \frac{y^2}{R^2}). \tag{B.3}$$

The definite integral can be calculated as

$$\int_{-R}^{R}(R^2-y^2)^{\frac{1}{3}}dy=\frac{4}{5}R^{\frac{5}{3}}\frac{\Gamma(\frac{3}{2})\Gamma(\frac{1}{3})}{\Gamma(1)\Gamma(\frac{5}{6})}=\frac{2}{5}\frac{\sqrt{\pi}\Gamma(\frac{1}{3})}{\Gamma(\frac{5}{6})}R^{\frac{5}{3}} \tag{B.4}$$

using the special value ${}_2F_1(a,b,c;1)=\frac{\Gamma(c)\Gamma(c-a-b)}{\Gamma(c-a)\Gamma(c-b)}$ [**48**]. This results in

$$M_R = D(c_I-c_0)\left(\frac{\beta}{D}\right)^{\frac{1}{3}}\frac{2^{\frac{2}{3}}\sqrt{\pi}3^{\frac{1}{3}}\Gamma(\frac{1}{3})}{5\Gamma(\frac{4}{3})\Gamma(\frac{5}{6})}R^{\frac{5}{3}} \tag{B.5}$$

$$=D(c_I-c_0)\pi R\left(\frac{\beta R^2}{D}\right)^{\frac{1}{3}}\frac{2^{\frac{2}{3}}3^{\frac{4}{3}}}{5\sqrt{\pi}\Gamma(\frac{5}{6})}= \qquad D(c_I-c_0)\frac{\pi}{2}R\left(\frac{4\beta R^2}{D}\right)^{\frac{1}{3}}2\frac{3^{\frac{4}{3}}}{5\sqrt{\pi}\Gamma(\frac{5}{6})}. \tag{B.6}$$

Setting $Pe=\frac{\beta R^2}{D}$ [**33**], we arrive at

$$M_R = D(c_I-c_0)\pi RSh \tag{B.7}$$

with [**32, 33**]

$$Sh=\frac{3^{\frac{4}{3}}2^{\frac{2}{3}}}{5\sqrt{\pi}\Gamma(\frac{5}{6})}Pe^{\frac{1}{3}}=\frac{2^{\frac{1}{3}}3^{\frac{4}{3}}\Gamma(\frac{1}{3})}{5\pi\Gamma(\frac{2}{3})}Pe^{\frac{1}{3}}\approx 0.68658Pe^{\frac{1}{3}}. \tag{B.8}$$

The thickness of the boundary layer can also be estimated from (A.15). For a circular electrode, the maximal length is $2R$, the maximal thickness of the boundary layer is

$$\delta^{\sharp}\approx= 3.694RPe^{-\frac{1}{3}}. \tag{B.9}$$

References

[1] C. M. A. Brett and A. M. F. C. O. Brett in *Compr. Chem. Kinet.*, ed. C. H. Bamford and R. G. Compton, Vol. 29; Elsevier Publ. Amsterdam-Oxford-NewYork-Tokyo, 1986.
[2] P. R. Unwin and R. G. Compton in *Compr. Chem. Kinet.*, Vol. 26; Elsevier Publ. Amsterdam-Oxford-NewYork-Tokyo, 1986.
[3] S. G. Weber and J. T. Long, *Anal. Chem.*, 1988, **60**, 903A–913A.
[4] H. Gerischer, I. Mattes, and R. Braun, *J. Electroanal. Chem.*, 1965, **10**, 553–567.
[5] P. R. Unwin and R. G. Compton, *J. Electroanal. Chem*, 1989, **274**, 249–256.
[6] R. G. Compton and P. R. Unwin, *J. Electroanal. Chem*, 1986, **205**, 1–20.
[7] N. Wakabayashi, H. Uchida, and M. Watanabe, *Electrochem. Solid-State Lett.*, 2002, **5**, E62–E65.
[8] T. H. Madden, N. Arvindan, and E. M. Stuve, *J. Electrochem. Soc.*, 2003, **150**, E1–E10.
[9] T. H. Madden and E. M. Stuve, *J. Electrochem. Soc.*, 2003, **150**, E571–E577.
[10] N. Wakabayashi, M. Takeichi, M. Itagaki, H. Uchida, and M. Watanabe, *J. Electroanal. Chem.*, 2005, **574**, 339–346.
[11] N. Wakabayashi, M. Takeichi, H. Uchida, and M. Watanabe, *J. Phys. Chem. B*, 2005, **109**, 5836–5841.
[12] Z. Jusys, J. Kaiser, and R. J. Behm, *Electrochim. Acta*, 2004, **49**, 1297–1305.
[13] Z. Jusys and R. J. Behm, *J. Phys. Chem. B*, 2004, **108**, 7893–7901.
[14] L. Colmenares, Z. Jusys, and R. J. Behm, *Langmuir*, 2006, **22**, 10437–10445.
[15] A. N. Frumkin, L. Nekrasov, V. G. Levich, and J. Ivanov, *J. Electroanal. Chem*, 1959, **1**, 84–90.
[16] V. G. Levich, *Physicochemical Hydrodynamics*, Prentice-Hall, Englewood Cliffs, N. J, 1962.
[17] Z. Jusys, H. Massong, and H. Baltruschat, *J. Electrochem. Soc.*, 1999, **146**, 1093–1098.
[18] Z. Jusys and R. J. Behm, *J. Phys. Chem. B*, 2001, **105**, 10874–10883.
[19] Z. Jusys and R. J. Behm, *Electrochim. Acta*, 2004, **49**, 3891–3900.
[20] M. Heinen, Y. X. Chen, Z. Jusys, and R. J. Behm, *Electrochim. Acta*, 2007, **52**, 5634–6543.
[21] M. Heinen, Y. X. Chen, Z. Jusys, and R. J. Behm, *Chem. Phys. Chem.*, 2007, **8**, 2484–2489.
[22] R. G. Compton, A. C. Fisher, R. G. Wellington, P. J. Dobson, and P. A. Leigh, *J. Phys. Chem*, 1993, **97**, 10410–10415.
[23] R. G. Compton, B. A. Coles, and A. C. Fisher, *J . Phys. Chem.*, 1994, **98**, 2441–2445.
[24] J. Fuhrmann, H. Zhao, E. Holzbecher, and H. Langmach, *Journal of Fuel Cell Science and Technology*, 2008, (in press).
[25] J. Divisek, J. Fuhrmann, K. Gärtner, and R. Jung, *J. Electrochem. Soc.*, 2003, **150**(6), A811–A825.
[26] J. Alden *Computational Electrochemistry* PhD thesis, Oxford Univ., 1998.
[27] M. Lourakis, levmar: Levenberg-Marquardt nonlinear least squares algorithms in C/C++ http://www.ics.forth.gr/lourakis/levmar/, 2004.
[28] E. Holzbecher, R. Halseid, Z. Jusys, J. Fuhrmann, and J. Behm In ed. FEMLAB GmbH, *Proc. COMSOL Anwenderkonferenz 2006*, pp. 112–115, Göttingen, 2006.
[29] T. J. Schmidt, H. A. Gasteiger, G. D. Stab, P. M. Urban, D. M. Kolb, and R. J. Behm, *J. Electrochem. Soc.*, 1998, **145**, 2354–2358.
[30] J. Jost, *Partial Differential Equations*, Springer, 2002.
[31] A. Lévêque, *Annales des Mines*, 1928, **13**, 201–299, 305–362, 381–415.
[32] L. P. Reiss and T. J. Hanratty, *A. I. Ch. E. J.*, 1963, p. 154.
[33] C. Phillips, *Quart. J. Mech. Appl. Math.*, 1990, **43**, 135–159.
[34] R. H. Macneal, *Quart. Math. Appl.*, 1953, **11**, 295–310.
[35] R. E. Bank and D. J. Rose, *SIAM Journal on Numerical Analysis*, 1987, **24**(4), 777–787.

[36] H. Si *Three-Dimensional Boundary Conforming Delaunay Mesh Generation* PhD thesis, Technical University Berlin, 2008.
[37] J. R. Shewchuk, triangle version 1.6 URL: http://www.cs.cmu.edu/˜quake/triangle.html, 2007.
[38] H. Si, TetGen version 1.4.2 URL: http://tetgen.berlios.de/, 2007.
[39] J. Fuhrmann and H. Langmach, *Appl. Numer. Math.*, 2001, **37**(1-2), 201–230.
[40] D. N. Allen and R. V. Southwell, *Quart. J. Mech. and Appl. Math.*, 1955, **8**, 129–145.
[41] K. Gärtner and R. Richter, *Nucl. Inst. Meth. Phys. Research A*, 2006, pp. 12–17.
[42] O. Schenk, K. Gärtner, G. Karypis, S. Röllin, and M. Hagemann, PARDISO - sparse direct solver URL: http://www.pardiso-project.org, 2007.
[43] H.-G. Roos, M. Stynes, and L. Tobiska, *Numerical Methods for Singularly Perturbed Differential Equations*, number 24 in Springer Series in Computational Mathematics, Springer, 1996.
[44] W. J. D. Blok and J. M. H. Fortuin, *Chem. Eng. Sci*, 1981, **36**, 1687–1694.
[45] G. Wedler, *Lehrbuch der Physikalischen Chemie*, VCH Verlagsgesellschaft mbH, 1985.
[46] S. Murad and S. Gupta, *Chem. Phys. Lett.*, 2000, **319**, 60–64.
[47] J. Newman and K. Thomas-Alyea, *Electrochemical Systems*, Wiley-Interscience, 2004.
[48] ed. M. Abramowitz and I. Stegun, *Handbook of Mathematical Functions*, number 55 in Applied Mathematics Series, National Bureau of Standards, 1972.
[49] S. Moshier, Cephes math library release 2.8 http://www.netlib.org/cephes/, 2000.
[50] Mathematica 5.0 Wolfram Research Inc., 2007.